

## Glycolytic Phenotype and AMP Kinase Modify the Pathologic Response of Tumor Xenografts to VEGF Neutralization

Giorgia Nardo<sup>1</sup>, Elena Favaro<sup>1</sup>, Matteo Curtarello<sup>2</sup>, Lidia Moserle<sup>1,3</sup>, Elisabetta Zulato<sup>2</sup>, Luca Persano<sup>1</sup>, Elisabetta Rossi<sup>1</sup>, Giovanni Esposito<sup>2</sup>, Marika Crescenzi<sup>2</sup>, Oriol Casanovas<sup>3</sup>, Ulrike Sattler<sup>4</sup>, Wolfgang Mueller-Klieser<sup>4</sup>, Barbara Biesalski<sup>4</sup>, Oliver Thews<sup>5</sup>, Rossella Canese<sup>6</sup>, Egidio Iorio<sup>6</sup>, Paola Zanovello<sup>1</sup>, Alberto Amadori<sup>1,2</sup>, and Stefano Indraccolo<sup>2</sup>

### Abstract

VEGF antagonists are now widely used cancer therapeutics, but predictive biomarkers of response or toxicity remain unavailable. In this study, we analyzed the effects of anti-VEGF therapy on tumor metabolism and therapeutic response by using an integrated set of imaging techniques, including bioluminescence metabolic imaging, 18-fluorodeoxyglucose positron emission tomography, and MRI imaging and spectroscopy. Our results revealed that anti-VEGF therapy caused a dramatic depletion of glucose and an exhaustion of ATP levels in tumors, although glucose uptake was maintained. These metabolic changes selectively accompanied the presence of large necrotic areas and partial tumor regression in highly glycolytic tumors. In addition, we found that the central metabolic protein kinase AMP-activated protein kinase (AMPK)—a cellular sensor of ATP levels that supports cell viability in response to energy stress—was activated by anti-VEGF therapy in experimental tumors. AMPK- $\alpha$ 2 attenuation increased glucose consumption, tumor cell sensitivity to glucose starvation, and tumor necrosis following anti-VEGF therapy. Taken together, our findings reveal functional links between the Warburg effect and the AMPK pathway with therapeutic responses to VEGF neutralization in tumor xenograft models. *Cancer Res*; 71(12); 4214–25. ©2011 AACR.

### Introduction

Tumor vascular targeting has been validated as a therapeutic concept with the approval of several drugs that block the VEGF-VEGF receptor (VEGFR) pathway (1, 2). However, both preclinical models and clinical trials have shown that benefits from first-generation angiogenesis inhibitors are generally short-term, because of the development of intrinsic as well as acquired resistance (3). A major challenge in the field is therefore to identify biomarkers of efficacy and toxicity that

guide the selection of patients who are most likely to benefit from treatment (4, 5).

Various types of response to antiangiogenic drugs such as sunitinib or bevacizumab have been observed in cancer patients. In some cases, patients present a decrease in tumor volume by more than 33%, qualifying them as partial responders according to RECIST criteria. In other patients, however, significant changes are observed only in tumor density with no decrease in size. This is often associated with central tumor cavitation and necrosis (6). Although this clinical observation suggests that antiangiogenic therapy may cause severe energy imbalance in certain tumors, it is currently unknown whether molecular or metabolic features of tumor cells could be involved in the type of pathologic response to VEGF-targeting drugs or could predict efficacy. Preclinical models may help to solve these issues.

In experimental tumors, anti-VEGF drugs typically prune the newly formed vasculature, thus reducing microvessel density (MVD), blood flow and perfusion, and eventually increasing the level of intratumoral hypoxia (7–9). Although in patients mechanisms might be more complex, considering that VEGF neutralization has therapeutic efficacy mainly when combined with conventional chemotherapy (10), it is currently held that following an initial time window of "vascular normalization," regression of tumor vasculature occurs leading to increased hypoxia (11). Less well understood is whether hypoxia eventually leads to tumor starvation. On one hand, hypoxia can exert both antiproliferative effects or induce cancer cell death depending on specific

**Authors' Affiliations:** <sup>1</sup>Department of Oncology and Surgical Sciences, Oncology Section, University of Padova; <sup>2</sup>Istituto Oncologico Veneto-IRCCS, Padova, Italy; <sup>3</sup>Translational Research Laboratory, Catalan Institute of Oncology, IDIBELL, L'Hospitalet de Llobregat, Spain; <sup>4</sup>Institute of Physiology and Pathophysiology, University Medical Center of the Johannes Gutenberg University, Mainz, Rhineland Palatinate; <sup>5</sup>Institute of Physiology, University of Halle, Saxony-Anhalt, Germany; and <sup>6</sup>Istituto Superiore di Sanità, Rome, Italy

**Note:** Supplementary data for this article are available at Cancer Research Online (<http://cancerres.aacrjournals.org/>).

Current address for E. Favaro: Molecular Oncology Laboratories, Weatherall Institute of Molecular Medicine, University of Oxford, John Radcliffe Hospital, Oxford, United Kingdom and for L. Persano: Department of Pediatrics "Salus Pueri," University of Padova, Padova, Italy.

**Corresponding Author:** Stefano Indraccolo, Istituto Oncologico Veneto-IRCCS, via Gattamelata, 64–35128 Padova, Italy. Phone: 39-049-8215875; Fax: 39-049-8072854; E-mail: stefano.indraccolo@unipd.it

doi: 10.1158/0008-5472.CAN-11-0242

©2011 American Association for Cancer Research.

genetic features of tumor cells (12–14). On the other hand, hypoxia can also favor invasion and metastasis, as an evasive mechanism to antiangiogenic therapy (reviewed in ref. 15).

Although it is usually granted that antiangiogenic drugs cut oxygen supply into tumors, surprisingly less is known about other metabolic perturbations induced by VEGF blockade in the tumor microenvironment.

In a previous study, we identified ovarian cancer cells endowed with different glycolytic phenotypes and correlated this feature with resistance or sensitivity to severe hypoxia *in vitro* (12). The great variations in glucose demand that we observed in these tumor cell lines possibly reflect their genetic heterogeneity and, importantly, this has also been observed in patients affected by the same tumor type, mainly by 18-fluorodeoxyglucose (FDG) positron emission tomography (PET; refs. 16, 17).

Xenografts obtained from these cells have been analyzed here to investigate the effects of VEGF neutralization on glucose metabolism by using, for the first time, an integrated imaging approach which included metabolic bioluminescence imaging, FDG PET, and magnetic resonance spectroscopy (MRS) analysis.

## Materials and Methods

### Cell culture and treatments

IGROV-1 cells were purchased from American Type Culture Collection; OC316 cells were provided by S. Ferrini (IST, Genoa, Italy). The human esophageal cancer cell line Kyse-30 (squamous cell carcinoma) and OE19 (adenocarcinoma) were purchased from European Collection of Animal Cell Cultures and used within 6 months from resuscitation. Kyse-30 cells were grown in RPMI 1640 + Ham's F12 medium (1:1) with 2% fetal calf serum (FCS) and 2 mmol/L glutamine. All other tumor cells were grown in RPMI 1640 medium (Euroclone) supplemented with 10% FCS (Life Technologies), 1% HEPES (10 mmol/L, Cambrex Bioscience), L-glutamine 2 mmol/L, and 1% antibiotics–antimycotic mix (Gibco-BRL). Cultures were maintained at 37°C in a humidified 5% CO<sub>2</sub>/95% air atmosphere. Where specified, IGROV-1 and OC316 cells were treated with 2-deoxyglucose (2DG; Sigma-Aldrich) at 6 g/L for 72 hours before apoptosis evaluation. To induce AMP-activated protein kinase (AMPK) pathway activation, tumor cells were stimulated with AICAR or Metformin (Sigma-Aldrich) at different concentrations for 24 hours before protein analysis. Hypoxic treatment (0.5% O<sub>2</sub>) was achieved by incubating cells in an InVivo2 300 hypoxic chamber (Ruskinn Technology).

### Animals and treatments

Procedures involving animals and their care conformed with institutional guidelines that comply with national and international laws and policies (EEC Council Directive 86/609, OJ L 358, 12 December, 1987). For tumor establishment, 8-week-old severe combined immunodeficient mice (SCID) mice (Charles River) were injected s.c. into both flanks with  $0.3 \times 10^6$  to  $0.5 \times 10^6$  tumor cells mixed at 4°C with liquid

Matrigel (Becton-Dickinson). Tumor volume (mm<sup>3</sup>) was calculated as previously reported (12). Anti-human VEGF monoclonal antibody (mAb; A4.6.1) was administered intraperitoneally (i.p.) at 100 µg/dose every 2 days, and mice were sacrificed 48 hours after the third treatment. Control mice received i.p. injections of PBS.

### Histology and immunohistochemistry

Quantification of necrosis was carried out by calculating the percentage of the necrotic area in the entire tumor section by using a light microscope equipped with digital camera and MODEL software (Leica Microsystems). pAMPK monoclonal (1:300 dilution, #2535S) and pACC polyclonal (1:400 dilution, #3661S) antibodies from Cell Signaling Technology were used for immunohistochemistry. Scoring of pAMPK or pACC expression was done by an experienced pathologist (G.E.) at a magnification of  $\times 100$ , on the basis of the Quick Score Method (18). Immunoreactivity was scored semiquantitatively for both the intensity and the proportion of cells staining: intensity was given scores 0 to 3 (no staining = 0, light staining = 1, moderate staining = 2, and strong staining = 3) and proportion was given scores 1 to 6 (0%–4% = 1, 5%–20% = 2, 21%–40% = 3, 41%–60% = 4, 61%–80% = 5, and 81%–100% = 6). The 2 scores were multiplied to obtain the final result of 0 to 18. In evaluation of pACC staining in RIP-Tag2 tumor sections, because of immunodetection heterogeneity among samples, the intensity of the normal tissue in each tissue section was taken as a reference to determine positivity/negativity of each tumor (total  $n = 116$ ) from 4 animals per treatment group. The percentage of positive tumors in each animal was calculated and graphed as average and SD in each treatment group. Mann-Whitney statistical test was used to determine significance  $P < 0.05$ .

### Evaluation of MVD and hypoxic areas

Tumor vessels were labeled with rat anti-CD31 mAb (1:50 dilution; Becton-Dickinson) followed by staining with a goat anti-rat 546 secondary antibody (Invitrogen) and quantification of MVD as detailed elsewhere (12). To identify hypoxic areas in tumors, we used pimonidazole hydrochloride (Hypox-probe-1; Chemicon International; ref. 12).

### MRI/MRS analysis

Subcutaneous xenografts derived from IGROV-1 and OC316 cells were characterized by MRI and quantitative MRS. Experiments were conducted on a Varian INOVA MRI/MRS system operating on small animals at 4.7 T (Varian) equipped with a transmitter volume RF coil actively decoupled from the receiver surface coil (RAPID Biomedical). Further details can be found in the Supplementary Data.

### Metabolic bioluminescence imaging

Excised tumors were cut into serial cryosections for structural hematoxylin and eosin (H&E) staining and bioluminescence measurements. For quantitative measurement of ATP and glucose, the method of metabolic imaging with induced bioluminescence was applied (19, 20). Further details can be found in the Supplementary Data.

### Animal PET studies

For  $\mu$ -PET measurements, tumors were implanted on the back of the thorax. Imaging was done when tumors reached a volume of 100 to 900  $\mu$ L. On the day of PET measurement, animals were anaesthetized with ketamine/xylazine and placed in prone position. The  $\mu$ -PET imaging was done on a microPET Focus 120 small animal PET (Siemens/Concorde). After a 15 minutes transmission scan with an external  $^{57}\text{Co}$  source, dynamic PET studies were acquired in two-dimensional mode.  $^{18}\text{F}$ -Fluorodeoxyglucose ( $^{18}\text{F}$ -FDG) with an activity of  $5.6 \pm 0.2$  MBq per animal was administered as a bolus injection of 0.2 mL via the tail vein. Time-activity curves were obtained with varying time frames (20s to 5 minutes) for a total measuring interval of 30 minutes. The PET listmode data were histogrammed into 13 frames and reconstructed by using OSEM algorithm. Volumes of interests were defined for the whole tumor, for necrotic areas of the tumor, and for reference tissue (soft tissue of the neck region). Ratios of vital tumor tissue (without necrosis) to reference tissue were calculated from integral image between 10 and 30 minutes after tracer injection.

### Statistical analysis

Results were expressed as mean value  $\pm$  SD. Statistical comparison between 2 sets of data was done by using either the unpaired Student's *t* test (2-tailed) or the Mann-Whitney test (2-tailed), depending on the distribution of values. Differences were considered statistically significant at  $P < 0.05$ .

Further experimental details are available in the Supplementary Data.

## Results

### Identification of tumor cells and xenografts with different metabolic features

On the basis of measurements of glucose consumption and lactate production rates *in vitro* as well as expression levels of glycolysis-associated genes, we recently identified OC316 and IGROV-1 cells as prototypes of highly and poorly glycolytic ovarian cancer cells, respectively (12). Interestingly, viability of OC316 but not of IGROV-1 cells was compromised under hypoxic conditions and glucose supplementation prevented cell death (12), thus suggesting that OC316 cells could be more dependent on glucose as energy substrate than IGROV-1 cells. To further validate this hypothesis, we measured cell viability following incubation under glucose starvation or with 2DG, an analog of glucose that binds and suppresses the glycolytic enzyme hexokinase II (21), and found reduced survival of OC316 cells compared with IGROV-1 cells (Supplementary Fig. S1A). Altogether, these results indicate that highly glycolytic OC316 cells are less able to cope with glucose deprivation than poorly glycolytic IGROV-1 cells. These metabolic features were further characterized by high resolution MRS, which showed higher intracellular concentration of lactate (Lac) in OC316 compared with IGROV-1 cells, as well as differences in the pool of glutamate and glutamine (Glx; Supplementary Fig. S1B).

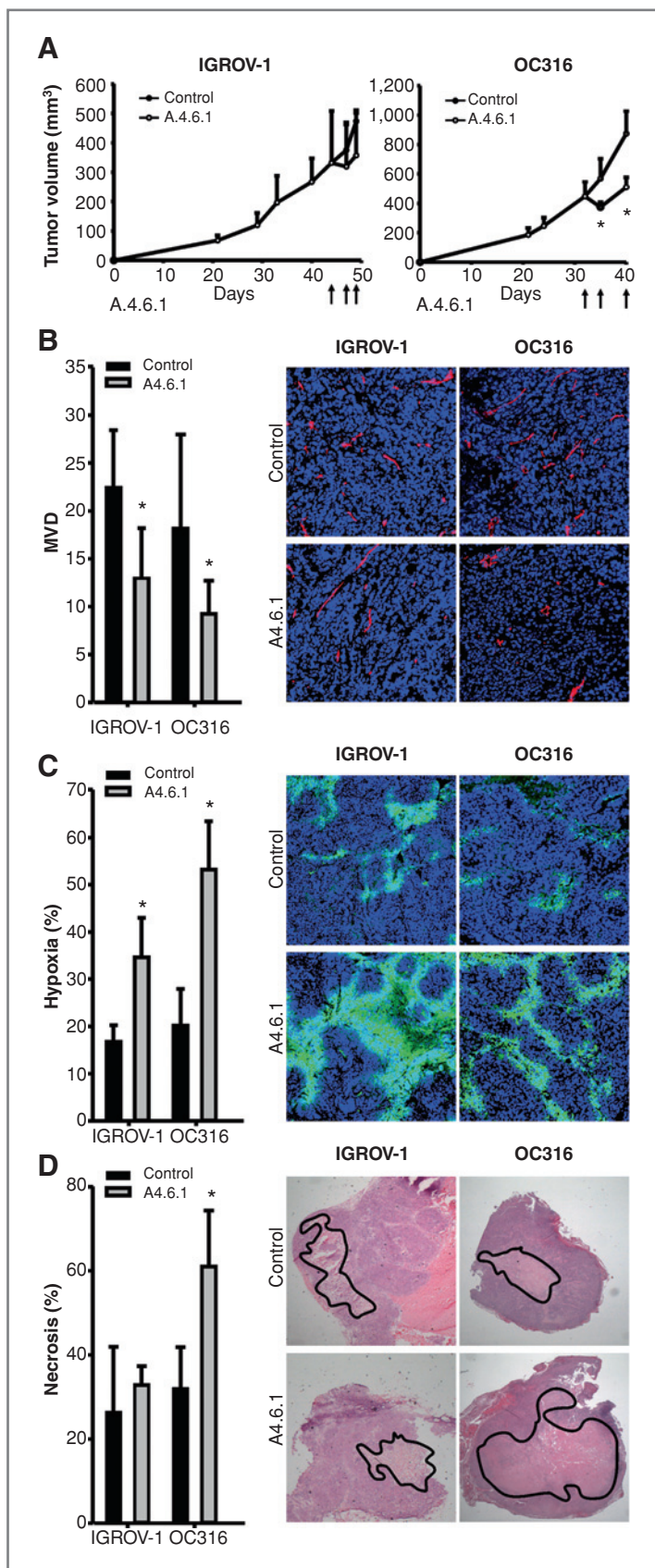
To determine whether these metabolic differences were conserved *in vivo*, we generated s.c. xenografts and characterized them by MRI and MRS. MRI can identify regions of necrosis or hemorrhage as hyperintense or hypointense areas, respectively, in the T2-weighted images. MRI revealed differences in tumor morphology and internal composition during growth between the 2 models: OC316 tumors were characterized by a prominent central necrotic core, whereas IGROV-1 tumors had several small and diffuse necrotic areas (Supplementary Fig. S1C). Following MRS analysis, lactate was observed in all OC316 tumors ( $n = 3$ ) and in 50% of the IGROV-1 xenografts analyzed ( $n = 4$ ). Mean lactate concentrations were  $38.2 \pm 8.3$  mmol/L in OC316 tumors and  $1.6 \pm 0.1$  mmol/L in IGROV-1 tumors (Supplementary Fig. S1D). Finally, quantitative PCR analysis indicated higher expression levels of *GAPDH*, *HKII*, and *LHDA* in OC316 compared with IGROV-1 tumors (Supplementary Fig. S1E). In summary, these findings indicate that OC316 and IGROV-1 are prototypes of tumors with markedly different glycolytic phenotypes.

### Outcome of anti-VEGF therapy in tumors with different metabolic properties

We subsequently treated OC316 and IGROV-1 xenografts with A4.6.1, a human VEGF neutralizing mAb bearing the same CDR region as bevacizumab (22). A significant reduction in tumor size was observed in OC316 but not in IGROV-1 tumors after 6 days of treatment (Fig. 1A). As expected, MVD was significantly reduced after anti-VEGF treatment in all tumors (Fig. 1B) and this was associated with a marked increase in hypoxic areas, as shown by quantification of pimonidazole adducts (Fig. 1C), and hypoxia inducible factor (HIF)-1 $\alpha$  levels (Supplementary Fig. S2). Histologic analysis showed large necrotic areas within OC316 tumors treated with A4.6.1, whereas minimal changes were measured in IGROV-1 tumors (Fig. 1D). This association between glycolytic phenotype and type of pathologic response to anti-VEGF therapy was not unique to the OC316/IGROV-1 pair. In fact, similar results were also seen after A4.6.1 administration to mice bearing Kyse-30 and OE19-derived tumors, formed by highly glycolytic and poorly glycolytic esophageal cancer cells, respectively (Supplementary Fig. S3).

The effects of VEGF neutralization in tumors were further documented by MRI techniques. The apparent diffusion coefficient (ADC) value is often correlated with tumor cellularity, and in experimental tumors, an elevated ADC value has been correlated with the necrotic fraction (23). Quantitative MRI analysis showed ADC values of  $8.0 \pm 3.8$  and  $7.3 \times 10^{-4} \pm 4.1 \times 10^{-4}$  mm<sup>2</sup>/s (mean  $\pm$  SD) for the OC316 and IGROV-1 xenografts, respectively, which were in good agreement with those recently measured in patients with ovarian carcinoma (24). Short-course anti-VEGF treatment was associated with changes in spectral profiles and ADC distributions. Treated OC316 tumors had a higher necrotic fraction compared with controls, as determined by an increase in ADC mean value ( $9.0 \pm 4.3$ ), because of an increase in the right wing of the ADC distribution (Fig. 2A). Differences in the spectral profile were also found, which could reflect changes in tumor environment (i.e., pH) and/or altered metabolism (Fig. 2B). The identity of these alterations remains

**Figure 1.** Anti-VEGF therapy increases necrosis of highly glycolytic tumors. **A**, kinetics of tumor development in SCID mice and effects of 3 injections of the anti-VEGF mAb A4.6.1 (arrows, 100  $\mu$ g/dose, administered every 2 days) on tumor size. \*,  $P < 0.05$  compared with the size of controls ( $n = 6$  mice per group). **B**, vascularization of tumors by staining with anti-CD31 mAb and calculation of MVD. Representative images (original magnification:  $\times 200$ ) are shown. Columns show mean  $\pm$  SD values ( $n = 5-10$  fields per tumor;  $n = 6$  tumors per group), \*  $P < 0.05$ . **C**, evaluation of hypoxia by pimonidazole adducts staining. Representative images (original magnification:  $\times 200$ ) are shown. Columns indicate quantitative analysis of hypoxic areas ( $n = 5-10$  fields per tumor;  $n = 6$  tumors per group), \*  $P < 0.05$ . **D**, histologic analysis shows larger necrotic areas in OC316 tumors compared with IGROV-1 tumors after A4.6.1. Representative images (original magnification:  $\times 25$ ) are shown. The continuous line marks the boards of necrotic tissue. Columns indicate quantitative analysis of necrotic areas in  $n = 5$  different tumors per group, \*  $P < 0.05$ .



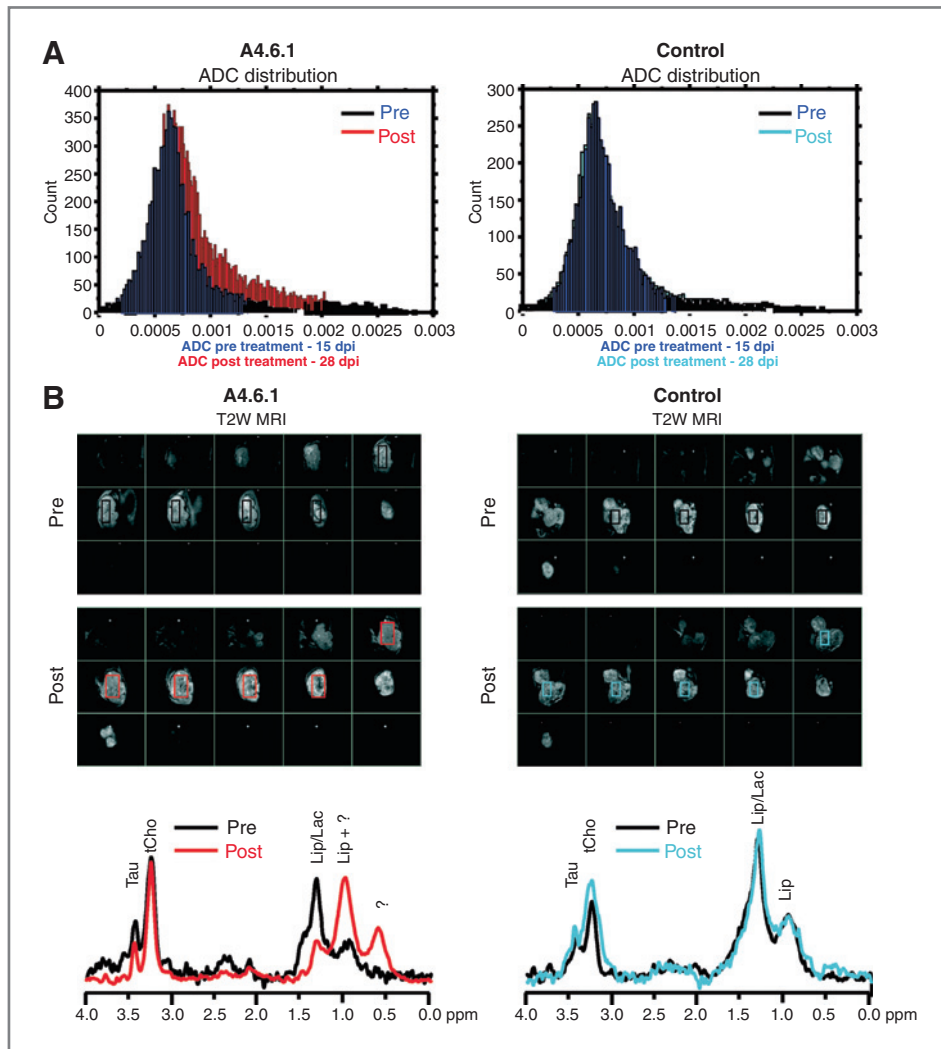


**Figure 2.** Morphometric and metabolic changes induced by anti-VEGF therapy in OC316 xenografts. **A**, ADC distributions showed an increase in the areas of necrosis (visible as the longer wing at the higher ADC values) in the A4.6.1-treated group compared with controls. **B**, top: T2-weighted images of OC316 xenografts pre (18 dpi) and 48 hours post (26 dpi) the third dose of anti-VEGF mAb (A4.6.1, 100  $\mu$ g/dose administered every other day). Controls received PBS injections. Bottom:  $^1\text{H}$  MR localized spectra (PRESS sequence, TR/TE = 4,000/272 ms) acquired from the voxels shown as blue or red rectangles in the images (ranging between 15 and 37  $\mu\text{L}$ ) at 18 (Pre) and 26 dpi (Post).

so far unknown. Twenty-four hours after the end of treatment, lactate was detected in all tumors (3/3,  $48 \pm 6$  mmol/L). On the other hand, treated IGROV-1 xenografts did not show any difference in the spectral profile with respect to untreated controls, whereas ADC distribution revealed a shift towards lower values in the treated group suggesting the presence of cell swelling (Supplementary Fig. S4).

#### Metabolic effects of anti-VEGF therapy

The large necrotic areas found in A4.6.1-treated OC316 xenografts suggested that acute VEGF neutralization caused bioenergetic perturbations. To investigate this, we carried out bioluminescence-based metabolic imaging of tumors, a technique which enables to visualize and measure steady-state levels of specific metabolites. Results shown in Figure 3A indicate a dramatic drop in glucose levels in OC316 xenografts following A4.6.1 administration compared with controls ( $1.36 \pm 0.61$   $\mu\text{mol/g}$  vs.  $3.36 \pm 1.48$   $\mu\text{mol/g}$ ). IGROV-1 tumors also disclosed significant reduction in glucose levels after treatment, albeit less intense compared with OC316 xeno-

grafts ( $2.91 \pm 1.21$   $\mu\text{mol/g}$  vs.  $3.89 \pm 1.67$   $\mu\text{mol/g}$ ; Fig. 3B). Moreover, ATP levels were also markedly reduced after A4.6.1 treatment, both in OC316 and IGROV-1 tumors (Fig. 3C). These findings show profound changes in glucose metabolism following acute VEGF neutralization in tumors.

#### Impact of anti-VEGF treatment on FDG uptake

PET imaging of OC316 tumors distinctly showed areas of reduced FDG uptake in the tumor center (Fig. 4A). These regions correspond to tissue necrosis found at MRI analysis and in H&E-stained tissue sections (Supplementary Fig. S1). For statistical analysis, these necrotic regions have not been taken into account. In IGROV-1 tumors, a rather homogeneous uptake was found (Fig. 4A). In these samples, FDG uptake normalized to the viable tumor volume was independent from anti-VEGF treatment as shown by the time-activity curves (Fig. 4B). The mean relative FDG uptake in the time interval from 10 to 30 minutes after tracer injection was  $173 \pm 12\%$  in A4.6.1-treated mice and  $175 \pm 12\%$  in control tumors (n.s.). However, in OC316 tumors treated with the anti-VEGF

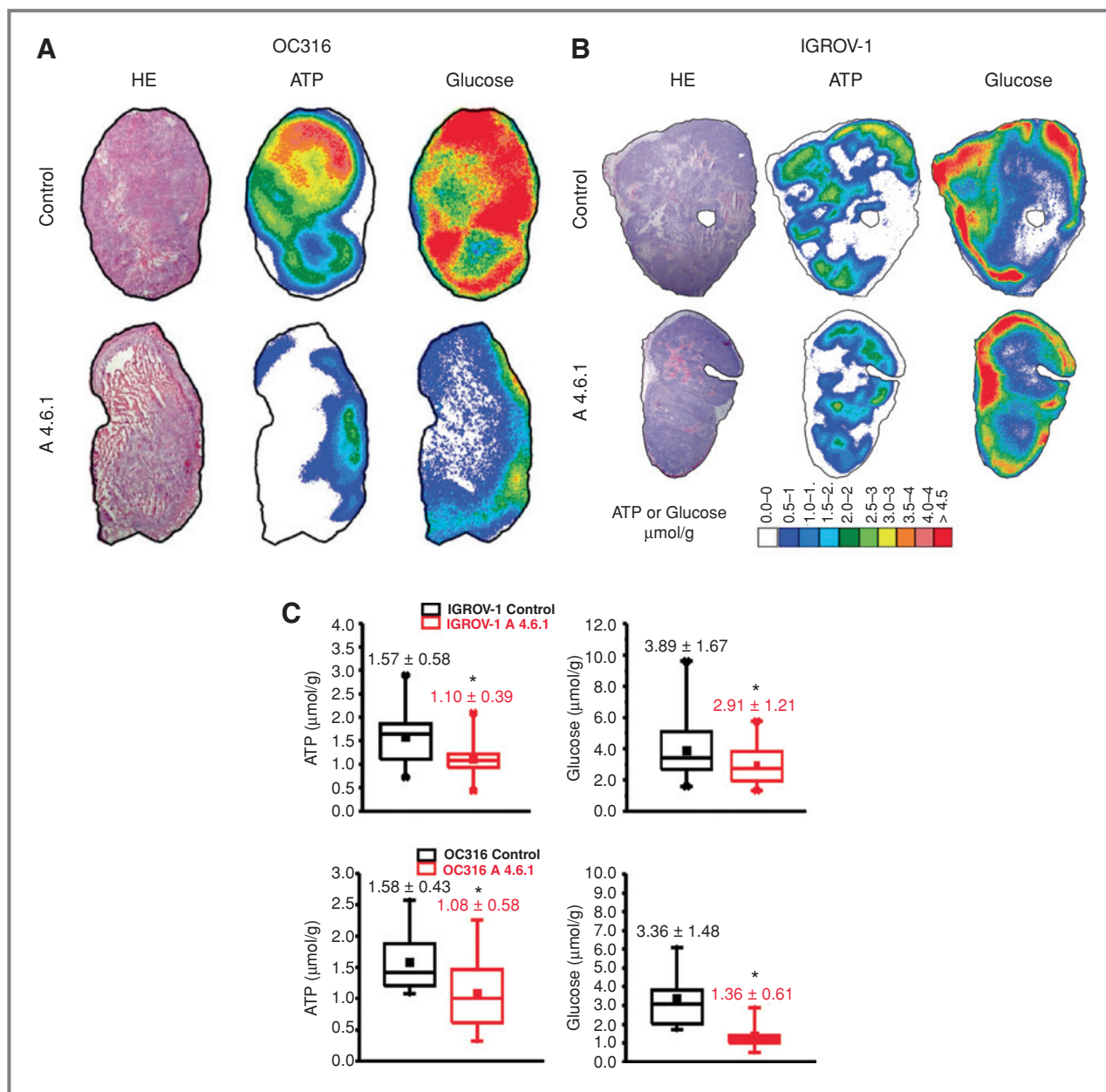


**Figure 3.** Metabolic effects of anti-VEGF therapy in tumors measured by bioluminescence imaging. A and B, H&E staining as well as color-coded distributions of ATP and glucose in sequential cryosections from representative OC316 and IGROV-1 tumors treated or not with the anti-VEGF mAb A4.6.1 (100 μg/dose, 3 doses given every other day). The concentration values were color-coded, with each color corresponding to a defined concentration range in μmol/g. C, metabolite concentrations in OC316 and IGROV-1 tumors treated or not with A4.6.1. Values were derived exclusively from vital tumor regions. ATP and glucose values were calculated from  $n = 12$ –32 sections from 4–10 different tumors.

antibody, PET imaging showed a significant higher glucose uptake as compared with untreated controls (Fig. 4B). The mean activity between 10 and 30 minutes was  $191 \pm 11\%$  (A4.6.1 treated) versus  $150 \pm 8\%$  (control;  $P < 0.01$ ). Altogether, these results indicate that glucose uptake is not compromised by anti-VEGF therapy, suggesting that the low glucose levels measured in tumors by bioluminescence-based metabolic imaging might depend on accelerated glucose consumption rather than impaired delivery.

### VEGF-targeting drugs induce AMPK activation in experimental tumors

AMPK is a cellular sensor that contributes to maintain the steady-state level of intracellular ATP (25). Because anti-VEGF treatment lowered both glucose and ATP *in vivo* (Fig. 3), we hypothesized that it might activate the AMPK pathway. Staining with an anti-pAMPK Ab disclosed variable AMPK activation in A4.6.1-treated tumors, showing much more intense expression of pAMPK in IGROV-1 compared with

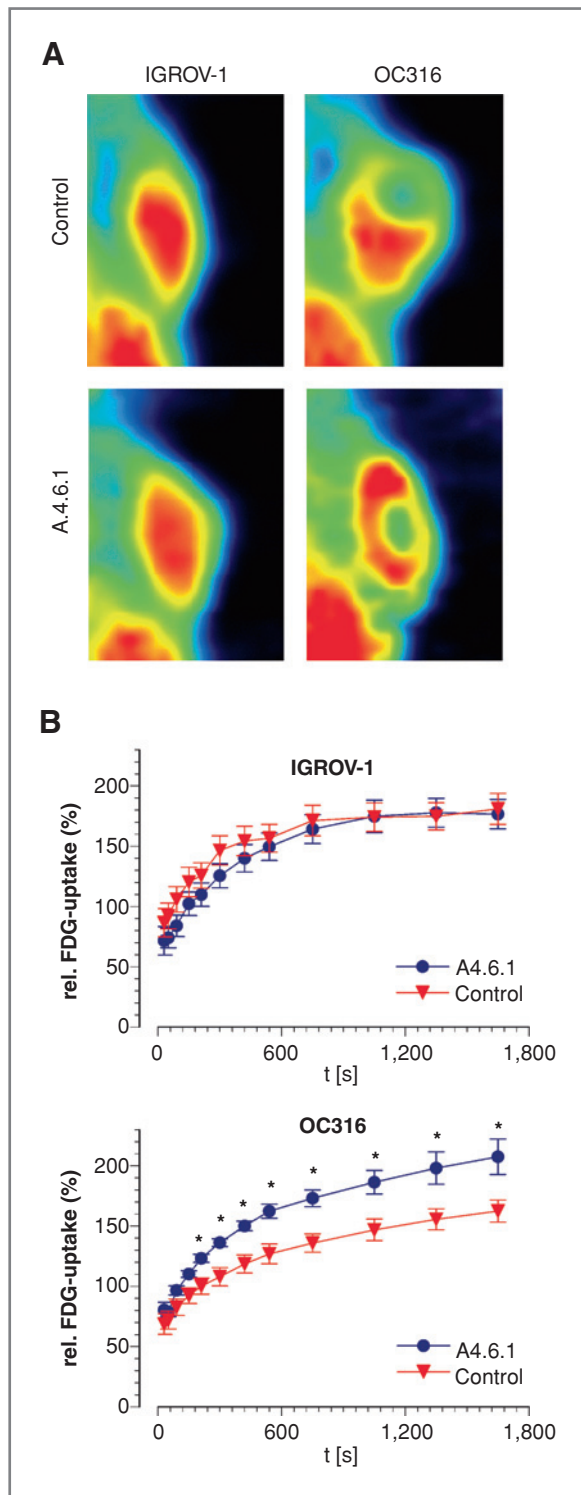


**Figure 4.** Effect of anti-VEGF treatment on  $^{18}\text{F}$ -FDG uptake in tumors measured by PET. **A**, representative PET images of IGROV-1 and OC316 tumors treated or not with the anti-VEGF mAb A4.6.1. In OC316 tumors, areas of reduced uptake in the center of the tissue can be identified. These areas correspond to extensive necrosis in these tumors. For further analysis, these regions have been excluded. **B**, time-activity curves of FDG uptake for IGROV-1 ( $n = 11$ ) and OC316 tumors ( $n = 12$ –16 samples). The uptake values per volume were normalized to a reference tissue (soft tissue of the neck region); data are expressed as mean  $\pm$  SEM; \*,  $P < 0.05$ .

OC316 tumors (Fig. 5A). Phosphorylation of acetyl-coenzyme A carboxylase (ACC), a key target of AMPK (26), was strongly increased in IGROV-1 tumors treated with anti-VEGF, compared with controls (Fig. 5B). In line with results of anti-pAMPK staining, OC316 tumors had very weak pACC signal, and this did not change in samples treated with anti-VEGF mAb (Fig. 5B). Moreover, treatment of IGROV-1 xenografts with vandetanib—an inhibitor of VEGFR, epidermal growth factor receptor, and RET tyrosine kinases (reviewed in ref. 27)—markedly increased pACC staining, further validating these findings (Fig. 5C).

Finally, strong pACC reactivity was also observed in RIP-Tag2 tumors treated either short or long term with DC101, an anti-VEGFR Ab (28), compared with controls (Fig. 5D), indicating that increased AMPK activation can occur as a consequence of VEGF blockade also in transgenic tumor models.

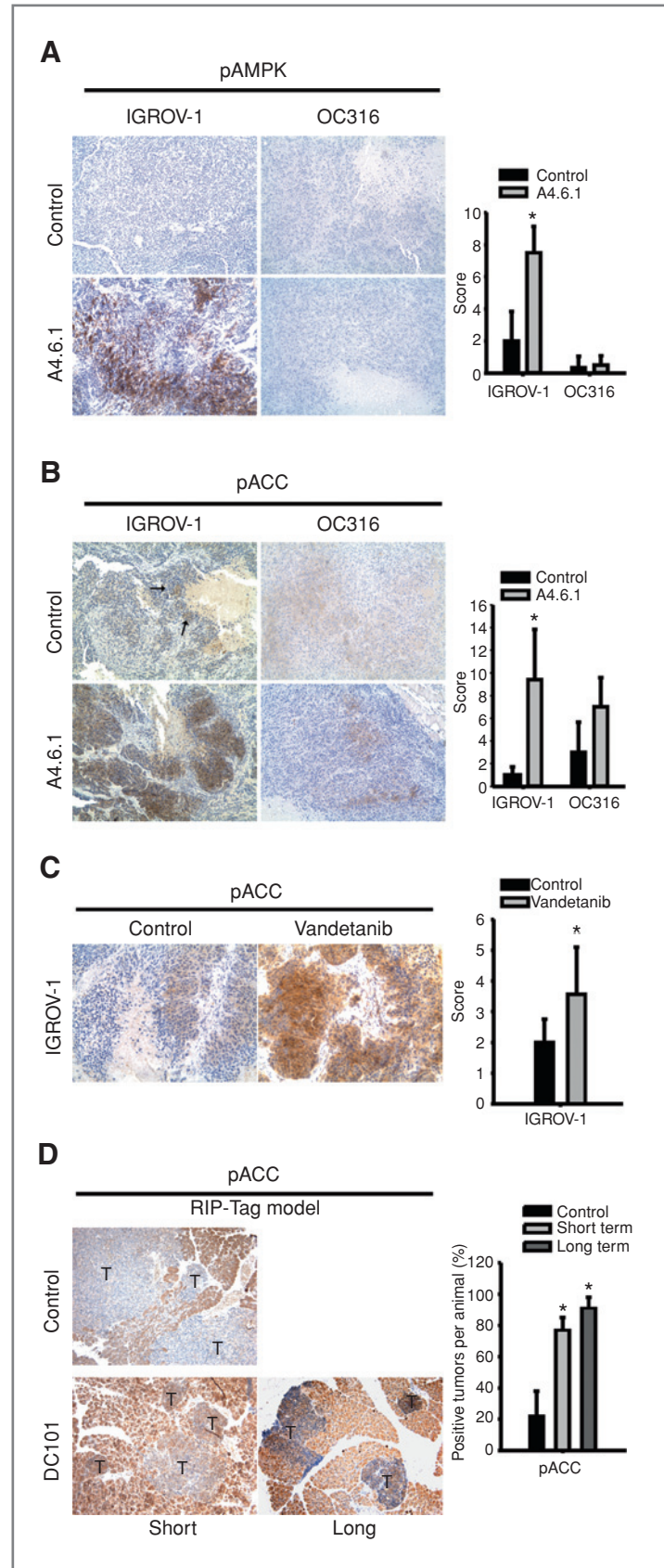
To further investigate the possibility that the AMPK pathway could be dysfunctional in OC316 cells, we measured AMPK activation in cells incubated under hypoxic conditions and/or glucose deprivation *in vitro*. Results indicate a raise in pAMPK levels in IGROV-1 but not OC316 cells following cultivation in the absence of glucose, both under normoxic and hypoxic conditions (Supplementary Fig. S5A). Analysis of pACC levels confirmed these findings, indicating strong ACC phosphorylation in IGROV-1 cells following glucose starvation, whereas pACC was only slightly increased in OC316 cells under the same experimental conditions (Supplementary Fig. S5A). To corroborate these results, IGROV-1 and OC316 cells were cultivated in the presence of canonical AMPK activators. AICAR, a direct AMPK activator (26), was able to activate AMPK in IGROV-1 but only barely in OC316 cells, as evaluated by immunoblotting analysis of pAMPK levels (Supplementary Fig. S5B). Similar results were obtained with Metformin, an indirect AMPK activator (Supplementary Fig. S5C).

Because AMPK is activated by liver kinase B1 (LKB1; ref. 29), we investigated expression levels of this kinase in tumor cells. Results show that LKB1 is expressed at apparently similar levels both in IGROV-1 and OC316 cells; in contrast, LKB1 was absent in HeLa cells, which are known to lack this kinase (ref. 30; Supplementary Fig. S6A). Immunofluorescence analysis, however, disclosed that the pattern of LKB1 intracellular staining was partially different in IGROV-1 compared with OC316 cells. In fact, LKB1 was invariably detected both in the cytoplasm and the nuclei of IGROV-1 cells, whereas  $30.11 \pm 8.68\%$  OC316 cells lacked cytoplasmic staining (Supplementary Fig. S6B). Sequencing of LKB1 disclosed a G > A variation at nucleotide 958 of LKB1 exon 8 (Supplementary Fig. S6C), which is predicted to introduce a valin to methionin change in a domain of LKB1 putatively involved in the formation of the multimeric complex of LKB1 with STRAD $\alpha$  and MO25 (31). Altogether, these findings indicate that the AMPK pathway is dysfunctional in OC316 cells, likely due to altered intracellular distribution of its upstream activator LKB1.

#### AMPK silencing modulates the response to anti-VEGF treatment

To conclusively prove involvement of AMPK in the response of tumors to anti-VEGF treatment, we silenced *AMPK* in

**Figure 5.** Anti-VEGF/R2 therapy increases AMPK activation in tumors. A and B, representative pictures of pAMPK and pACC staining of xenografts following treatment with the anti-VEGF mAb A4.6.1 (100  $\mu$ g/dose, 3 doses given every 2 days). Arrows indicate pACC-positive areas in control tumors. Right, scoring of pAMPK- or pACC-positive areas in  $n = 6$  different tumors for each group. \*,  $P < 0.01$ . C, analysis of pACC staining of IGROV-1 xenografts following treatment with vandetanib (50 mg/kg/day for 3 days). Right, scoring of pACC-positive areas in  $n = 7$  different tumors for each group. \*,  $P < 0.01$ . D, analysis of ACC activation in RIP-Tag2 tumors treated for 1 week (short term) or 4 continuous weeks (long term) with anti-mVEGFR2 antibody (DC101). Left, representative pictures of pACC immunohistochemical detection are shown for each treatment group. T, individual tumors. Right, quantification of the percentage of pACC-positive tumors per animal in each treatment group. A total of 116 tumors were scored, from 4 independent animals per treatment group. \*,  $P < 0.05$ .



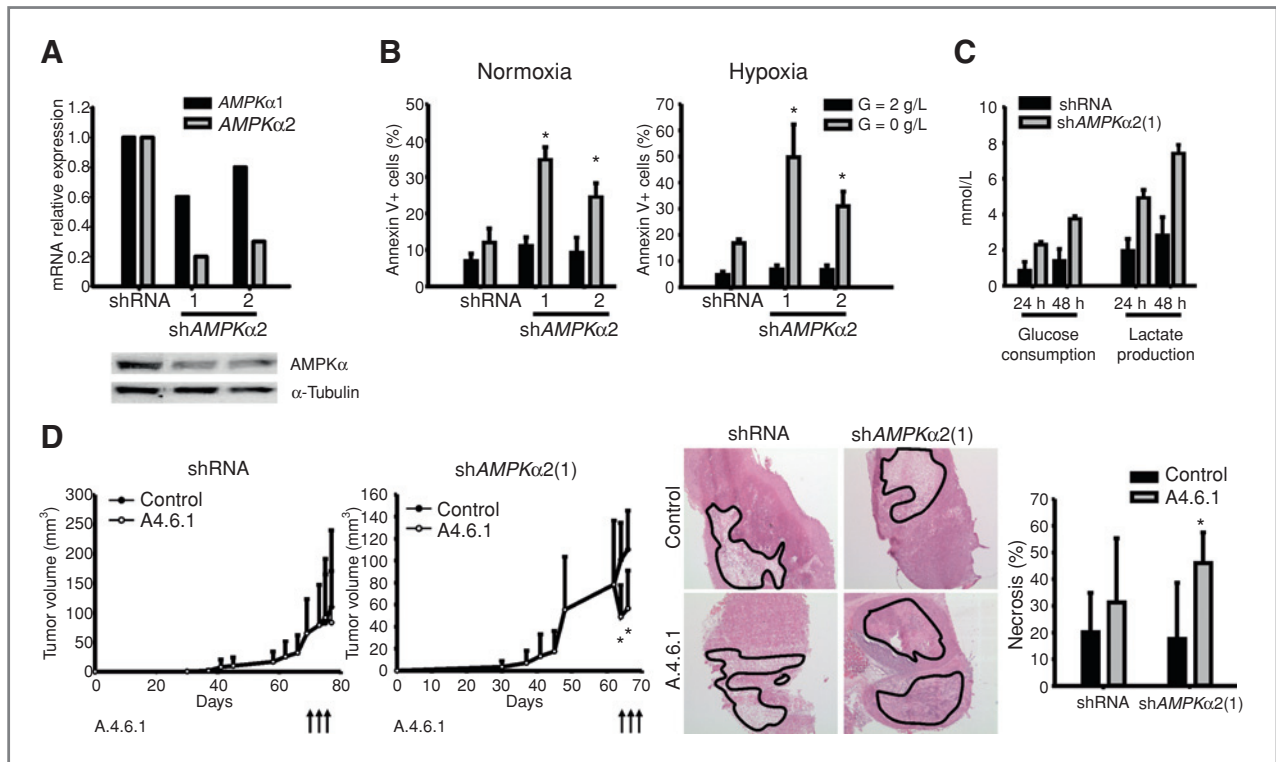


**Figure 6.** AMPK $\alpha$ 2 silencing increases tumor cell death under glucose starvation and modulates the *in vivo* response to anti-VEGF therapy. **A**, transduction of IGROV-1 cells with lentiviral vectors encoding 2 different shRNA-targeting AMPK $\alpha$ 2 (shAMPK $\alpha$ 2) modulates AMPK $\alpha$  mRNA (top) and protein (bottom) expression levels, compared with controls (shRNA). Similar findings were obtained in 2 additional independent experiments. **B**, measurements of apoptosis by Annexin V staining of IGROV-1 cells bearing reduced AMPK $\alpha$ 2 levels under glucose starvation. Experiments were conducted either under normoxic or hypoxic (0.5% pO<sub>2</sub>) conditions. Columns report the mean values  $\pm$  SD of 4 independent experiments. \*,  $P < 0.05$ , compared with shRNA values. **C**, measurement of glucose consumption and lactate production. Cells were plated in P6 wells at  $1.5 \times 10^5$  cells per well, incubated for 24 and 48 hours *in vitro* under normoxic conditions and metabolic parameters quantified by an automatic analyzer. Mean  $\pm$  SD of 3 experiments is shown. \*,  $P < 0.05$ . **D**, AMPK $\alpha$ 2 attenuation is associated with increased necrosis following anti-VEGF therapy. Subcutaneous tumor growth curves and measurement of tumor size are shown in the left ( $n = 6$  tumors pergroup). Histologic analysis (right) disclosed large necrotic areas in shAMPK $\alpha$ 2(1) IGROV-1 tumors after A4.6.1 administration. Representative images (original magnification:  $\times 200$ ) are shown. The continuous line marks the boards of necrotic tissue. Columns indicate quantitative analysis of necrotic areas in  $n = 6$  different tumors of each group. \*,  $P < 0.05$ .

IGROV-1 cells, which have a functional AMPK pathway. Although IGROV-1 cells express both AMPK $\alpha$ 1 and AMPK $\alpha$ 2 isoforms, we tested the effects of AMPK $\alpha$ 2 silencing, because previous data showed the dominant role of this isoform in determining the balance between proliferation and cell death in ovarian cancer (32). Following transduction of 2 different lentiviral vectors encoding AMPK $\alpha$ 2-specific short-hairpin RNA (shRNA), expression of AMPK $\alpha$ 2 transcript was reduced by 70% to 90% compared with control. Moreover, AMPK $\alpha$ 1 expression was also attenuated by 20% to 40% (Fig. 6A). Western blot analysis confirmed the presence of reduced AMPK level in these cells (Fig. 6A), referred to here as IGROV-1 shAMPK $\alpha$ 2 cells. Proliferation (Supplementary Fig. S7) and viability (Fig. 6B) of IGROV-1 shAMPK $\alpha$ 2 cells under standard culture conditions were similar to that of control cells, transduced with a scramble shRNA vector. However, glucose starvation was associated with significantly higher death of IGROV-1 shAMPK $\alpha$ 2 compared with control cells (Fig. 6B). Intriguingly, attenuation of AMPK $\alpha$ 2 was followed by a marked increase in glucose consumption and lactate production under normoxic conditions (Fig. 6C),

implying that AMPK levels modulate the glycolytic rate in IGROV-1 cells.

*In vivo*, xenografts derived from IGROV-1 shAMPK $\alpha$ 2 cells developed at faster rates compared with controls (Fig. 6D). Following treatment with A4.6.1, a significant increase in necrosis was measured in tumors formed by IGROV-1 shAMPK $\alpha$ 2 cells, whereas no difference was measured in control tumors (Fig. 6D). Altogether, these findings show that AMPK levels are critical to modulate the morphologic responses of tumors to VEGF neutralization.

## Discussion

Here, we investigated how metabolic parameters contribute to determine the pathologic response to VEGF blockade in tumor xenografts. A first conclusion is that the glycolytic rate in cultured cell lines and their level of "glucose addiction" are of paramount importance in determining the amount of necrosis caused by angiogenesis inhibition. Although it is well recognized that low glucose concentrations can be present in large solid tumors because of their compromised vascular

functions (20, 33), with regard to the effects of antiangiogenic drugs, previous studies have mainly characterized changes in hypoxia, assuming that glucose would remain available because of its high diffusion capacity in tissues. Our metabolic imaging results clearly showed that VEGF blockade acutely perturbs glucose and ATP levels in xenografts. Because in PET experiments FDG uptake in A4.6.1-treated animals was either the same (IGROV-1) or even higher (OC316) than in untreated controls (Fig. 4B), glucose supply does not seem to be impaired by short-term anti-VEGF treatment. The higher FDG uptake into A4.6.1-treated OC316 tumors may be the result of either a higher glucose consumption rate or the induction of GLUT transporters which facilitate cellular uptake. Both mechanisms may depend from hypoxia-induced HIF-1 $\alpha$  accumulation, which was indeed detected in A4.6.1-treated tumors (Supplementary Fig. S2). Although PET findings may seem to contradict those of bioluminescence-based metabolic imaging, it should be stressed that one method measures glucose uptake and the other steady-state levels. Therefore, it is possible that glucose consumption in anti-VEGF-treated animals exceeds the increased glucose uptake, resulting in lower steady-state levels of this metabolite.

Metabolic imaging also showed that anti-VEGF treatment caused similar drops in mean ATP levels in OC316 and IGROV-1 xenografts. Therefore, quantitative variations in ATP levels are not likely to account for the different levels of necrosis detected in OC316 versus IGROV-1 xenografts.

A second key finding of the study is the demonstration that VEGF blockade increased AMPK activation in tumors, as shown by immunohistochemistry analysis of pAMPK and pACC levels, both in xenografts of ovarian cancer cells treated with 2 different angiogenesis inhibitors and in spontaneous tumors arising in RIP-Tag2 transgenic mice (Fig. 5). AMPK is a central metabolic switch found in all eukaryotes that governs glucose and lipid metabolism in response to alterations in nutrients and intracellular energy levels, as well as cell polarity (29). The serine-threonine kinase LKB1, a known tumor suppressor, is a key upstream activator of AMPK (29). Because AMPK is activated when intracellular levels of ATP decline and intracellular levels of AMP increase, such as during nutrient deprivation and hypoxia, a certain level of AMPK activation is commonly seen in solid tumors (34), and we also observed this in the perinecrotic areas of our control xenografts (Fig. 5). In our study, however, hypoxia did not activate AMPK *in vitro* unless tumor cells were grown under glucose starvation (Supplementary Fig. S5). Therefore, AMPK activation after VEGF blockade is not likely to depend directly on hypoxia but, rather, on the low glucose and ATP levels detected in tumors. Indeed, AMPK activation fits nicely with the results of bioluminescence imaging. AMPK deficiency promotes apoptosis in culture following treatment with energy stress-inducing agents (30, 35), probably because cells cannot restore ATP levels. It is thus possible that defects of AMPK activation may in part account for the reduced survival of OC316 cells under glucose starvation or 2DG treatment *in vitro*, as well as after antiangiogenic therapy *in vivo*. The finding of a V320M variation in the LKB1 domain involved in interaction with STRAD $\alpha$  (31) might affect LKB1

trafficking and could putatively explain the predominantly nuclear localization of LKB1 in these cells, as well as its reduced activity (36). Importantly, attenuation of AMPK $\alpha$ 2 in IGROV-1 cells was sufficient to modulate their survival under glucose starvation *in vitro* and to increase the level of necrosis in xenografts treated with the anti-VEGF mAb, thus lending support to this hypothesis.

We also noticed that AMPK $\alpha$ 2 attenuation increased glucose consumption and lactate production by IGROV-1 cells, thus contributing to the Warburg effect. It was previously known that HIF1 $\alpha$  and its target genes are upregulated in LKB1-, AMPK-, and TSC-deficient fibroblasts, indicating that loss of any of these genes is sufficient to alter cell metabolism (37, 38). In IGROV-1 cells, HIF1 $\alpha$  activity measured by a luciferase-based reporter assay doubled following attenuation of AMPK $\alpha$ 2 levels by shRNA (Supplementary Fig. S8), suggesting that HIF1 $\alpha$  could in part contribute to the modulation of cell metabolism in this system. The observation that AMPK is dysfunctional in OC316 cells may also in part explain their increased glycolytic phenotype compared with IGROV-1 cells, although we are aware that also other signaling pathways dysregulated in cancer—including c-myc, KRAS, Akt, and p53—may regulate glucose metabolism (39). In this regard, it is important to stress that Akt phosphorylation at residues ser473 and thr308 was lower in OC316 compared with IGROV-1 cells (Supplementary Fig. S9). Thus, although it has been reported that cells with high Akt activity do not activate AMPK efficiently (40), this mechanism is not likely involved in OC316 cells.

This study clearly has translational implications both for ovarian cancer and other malignancies. Bevacizumab has therapeutic activity in ovarian cancer also as single agent (41, 42) and 2 large-phase III clinical trials (GOG-218 and ICON7) are undergoing to establish whether it improves efficacy of standard chemotherapy (43, 44). Our findings are potentially important for several reasons: First, they identify both AMPK activation and the glycolytic phenotype of tumors as novel biomarkers of pathologic response to anti-VEGF therapy, although further work will be required to validate these concepts and to determine their predictive value in patients. Second, our findings may offer an interpretation of the molecular mechanisms underlying certain toxic effects of VEGF blockade, including GI perforations and bleeding. GI perforations have been reported in as high as 11.4% of patients with metastatic ovarian cancer treated with bevacizumab (42) and occur more frequently in subjects with more advanced stage disease showing tumor involvement of the intestinal wall. Life-threatening bleeding has been reported in about 2.3% to 10% of patients with metastatic non-small cell lung cancer (NSCLC) treated with bevacizumab and chemotherapy and squamous histology and tumor cavitation before or during bevacizumab treatment remain the only known risk factors (45). It will be important to test whether highly glycolytic tumors or tumors bearing defects in LKB1/AMPK are associated with these serious side effects, particularly in NSCLC, in which LKB1 mutations are common (46).

Finally, our study has highlighted the potential of MRI/MRS analysis for noninvasive metabolic characterization of tumors,

which is important because it is generally difficult to obtain biopsies from cancer patients subjected to antiangiogenic therapy. The MRS approach adopted in this work, although liable to overestimation because of possible residual lipid contamination, has already been applied to tumors in patients (47). *In vivo* detection of lactate levels and alterations following anti-VEGF treatment by MRS in combination with MRI could represent noninvasive tools to identify "glucose addicted" tumors and correlate this with AMPK function and clinical responses to bevacizumab and other antiangiogenic drugs.

### Disclosure of Potential Conflicts of Interests

The authors have no conflicts of interest to declare.

### Authors' Contributions

G. Nardo and E. Favaro contributed equally to this work.

### References

- Cao Y. Angiogenesis: what can it offer for future medicine? *Exp Cell Res* 2010;316:1304–8.
- Heath VL, Bicknell R. Anticancer strategies involving the vasculature. *Nat Rev Clin Oncol* 2009;6:395–404.
- Bergers G, Hanahan D. Modes of resistance to anti-angiogenic therapy. *Nat Rev Cancer*; 8:592–603.
- Cao Y. Off-tumor target–beneficial site for antiangiogenic cancer therapy? *Nat Rev Clin Oncol* 2010;7:604–8.
- Jain RK, Duda DG, Willett CG, Sahani DV, Zhu AX, Loeffler JS, et al. Biomarkers of response and resistance to antiangiogenic therapy. *Nat Rev Clin Oncol* 2009;6:327–38.
- Favre S, Demetri G, Sargent W, Raymond E. Molecular basis for sunitinib efficacy and future clinical development. *Nat Rev Drug Discov* 2007;6:734–45.
- Fenton BM, Paoni SF, Ding I. Effect of VEGF receptor-2 antibody on vascular function and oxygenation in spontaneous and transplanted tumors. *Radiother Oncol* 2004;72:221–30.
- Franco M, Man S, Chen L, Emmenegger U, Shaked Y, Cheung AM, et al. Targeted anti-vascular endothelial growth factor receptor-2 therapy leads to short-term and long-term impairment of vascular function and increase in tumor hypoxia. *Cancer Res* 2006;66:3639–48.
- Winkler F, Kozin SV, Tong RT, Chae SS, Booth MF, Garkavtsev I, et al. Kinetics of vascular normalization by VEGFR2 blockade governs brain tumor response to radiation: role of oxygenation, angiopoietin-1, and matrix metalloproteinases. *Cancer Cell* 2004;6:553–63.
- Grothey A, Galanis E. Targeting angiogenesis: progress with anti-VEGF treatment with large molecules. *Nat Rev Clin Oncol* 2009;6:507–18.
- Jain RK, Duda DG, Clark JW, Loeffler JS. Lessons from phase III clinical trials on anti-VEGF therapy for cancer. *Nat Clin Pract Oncol* 2006;3:24–40.
- Favaro E, Nardo G, Persano L, Masiero M, Moserle L, Zamarchi R, et al. Hypoxia inducible factor-1 $\alpha$  inactivation unveils a link between tumor cell metabolism and hypoxia-induced cell death. *Am J Pathol* 2008;173:1186–201.
- Papandreou I, Krishna C, Kaper F, Cai D, Giaccia AJ, Denko NC. Anoxia is necessary for tumor cell toxicity caused by a low-oxygen environment. *Cancer Res* 2005;65:3171–8.
- Steinbach JP, Wolburg H, Klump A, Probst H, Weller M. Hypoxia-induced cell death in human malignant glioma cells: energy deprivation promotes decoupling of mitochondrial cytochrome c release from caspase processing and necrotic cell death. *Cell Death Differ* 2003;10:823–32.
- Ebos JM, Lee CR, Kerbel RS. Tumor and host-mediated pathways of resistance and disease progression in response to antiangiogenic therapy. *Clin Cancer Res* 2009;15:5020–5.
- Avril N, Rose CA, Schelling M, Dose J, Kuhn W, Bense S, et al. Breast imaging with positron emission tomography and fluorine-18 fluoro-deoxyglucose: use and limitations. *J Clin Oncol* 2000;18:3495–502.
- Higashi K, Ueda Y, Sakurai A, Wang XM, Xu L, Murakami M, et al. Correlation of Glut-1 glucose transporter expression with [<sup>18</sup>F]FDG uptake in non-small cell lung cancer. *Eur J Nucl Med* 2000;27:1778–85.
- Hadad SM, Baker L, Quinlan PR, Robertson KE, Bray SE, Thomson G, et al. Histological evaluation of AMPK signalling in primary breast cancer. *BMC Cancer* 2009;9:307.
- Walenta S, Schroeder T, Mueller-Klieser W. Metabolic mapping with bioluminescence: basic and clinical relevance. *Biomol Eng* 2002;18:249–62.
- Walenta S, Schroeder T, Mueller-Klieser W. Lactate in solid malignant tumors: potential basis of a metabolic classification in clinical oncology. *Curr Med Chem* 2004;11:2195–204.
- Xu RH, Pelicano H, Zhou Y, Carew JS, Feng L, Balla KN, et al. Inhibition of glycolysis in cancer cells: a novel strategy to overcome drug resistance associated with mitochondrial respiratory defect and hypoxia. *Cancer Res* 2005;65:613–21.
- Gerber HP, Ferrara N. Pharmacology and pharmacodynamics of bevacizumab as monotherapy or in combination with cytotoxic therapy in preclinical studies. *Cancer Res* 2005;65:671–80.
- Morse DL, Galons JP, Payne CM, Jennings DL, Day S, Xia G, et al. MRI-measured water mobility increases in response to chemotherapy via multiple cell-death mechanisms. *NMR Biomed* 2007;20:602–14.
- Sala E, Priest AN, Kataoka M, Graves MJ, McLean MA, Joubert I, et al. Apparent diffusion coefficient and vascular signal fraction measurements with magnetic resonance imaging: feasibility in metastatic ovarian cancer at 3 Tesla: technical development. *Eur Rad* 2010;20:491–6.
- Carling D. The AMP-activated protein kinase cascade—a unifying system for energy control. *Trends Biochem Sci* 2004;29:18–24.
- Hardie DG. AMP-activated protein kinase as a drug target. *Annu Rev Pharmacol Toxicol* 2007;47:185–210.
- Morabito A, Piccirillo MC, Falasconi F, De Feo G, Del Giudice A, Bryce J, et al. Vandetanib (ZD6474), a dual inhibitor of vascular endothelial growth factor receptor (VEGFR) and epidermal growth factor receptor (EGFR) tyrosine kinases: current status and future directions. *Oncologist* 2009;14:378–90.
- Paez-Ribes M, Allen E, Hudock J, Takeda T, Okuyama H, Vinals F, et al. Antiangiogenic therapy elicits malignant progression of tumors to increased local invasion and distant metastasis. *Cancer Cell* 2009;15:220–31.
- Shackelford DB, Shaw RJ. The LKB1-AMPK pathway: metabolism and growth control in tumour suppression. *Nat Rev Cancer* 2009;9:563–75.

### Acknowledgments

We thank Genentech, Inc. for providing the A4.6.1 anti-VEGF mAb. We thank P. Fogar (Azienda Ospedaliera di Padova, Padova, Italy) for lactate/glucose measurements. We also thank F. Podo (Istituto Superiore di Sanità, Rome, Italy) for stimulating discussions of these data.

### Grant Support

This work was supported by grants from AIRC and FIRC; Ministry of University and Research, 60% and PRIN; Ministry of Health, Oncology Program 2006; Banco Popolare di Verona, Progetto Oncologico di Medicina Molecolare: i tumori femminili; Università di Padova–Progetto d'Ateneo 2010–and from the Deutsche Forschungsgemeinschaft DFG (Mu 576/15-1 and SA 1749/3-1) and from the Mainzer Forschungsfoerderungprogramm MAIFOR (#8277000).

The costs of publication of this article were defrayed in part by the payment of page charges. This article must therefore be hereby marked *advertisement* in accordance with 18 U.S.C. Section 1734 solely to indicate this fact.

Received January 24, 2011; revised April 7, 2011; accepted April 19, 2011; published OnlineFirst May 5, 2011.

30. Shaw RJ, Kosmatka M, Bardeesy N, Hurler RL, Witters LA, DePinho RA, et al. The tumor suppressor LKB1 kinase directly activates AMP-activated kinase and regulates apoptosis in response to energy stress. *Proc Natl Acad Sci USA* 2004;101:3329–35.
31. Zeqiraj E, Filippi BM, Deak M, Alessi DR, van Aalten DM. Structure of the LKB1-STRAD-MO25 complex reveals an allosteric mechanism of kinase activation. *Science* 2009;326:1707–11.
32. Hallstrom TC, Mori S, Nevins JR. An E2F1-dependent gene expression program that determines the balance between proliferation and cell death. *Cancer Cell* 2008;13:11–22.
33. Vaupel P. Tumor microenvironmental physiology and its implications for radiation oncology. *Semin Radiat Oncol* 2004;14:198–206.
34. Laderoute KR, Amin K, Calaoagan JM, Knapp M, Le T, Orduna J, et al. 5'-AMP-activated protein kinase (AMPK) is induced by low-oxygen and glucose deprivation conditions found in solid-tumor microenvironments. *Mol Cell Biol* 2006;26:5336–47.
35. Carretero J, Medina PP, Blanco R, Smit L, Tang M, Roncador G, et al. Dysfunctional AMPK activity, signalling through mTOR and survival in response to energetic stress in LKB1-deficient lung cancer. *Oncogene* 2007;26:1616–25.
36. Boudeau J, Baas AF, Deak M, Morrice NA, Kieloch A, Schutkowski M, et al. MO25alpha/beta interact with STRADalpha/beta enhancing their ability to bind, activate and localize LKB1 in the cytoplasm. *EMBO J* 2003;22:5102–14.
37. Brugarolas JB, Vazquez F, Reddy A, Sellers WR, Kaelin WG, Jr. TSC2 regulates VEGF through mTOR-dependent and -independent pathways. *Cancer Cell* 2003;4:147–58.
38. Shackelford DB, Vasquez DS, Corbeil J, Wu S, Leblanc M, Wu CL, et al. mTOR and HIF-1alpha-mediated tumor metabolism in an LKB1 mouse model of Peutz-Jeghers syndrome. *Proc Natl Acad Sci USA* 2009;106:11137–42.
39. Vander Heiden MG, Cantley LC, Thompson CB. Understanding the Warburg effect: the metabolic requirements of cell proliferation. *Science* 2009;324:1029–33.
40. Buzzai M, Bauer DE, Jones RG, Deberardinis RJ, Hatzivassiliou G, Elstrom RL, et al. The glucose dependence of Akt-transformed cells can be reversed by pharmacologic activation of fatty acid beta-oxidation. *Oncogene* 2005;24:4165–73.
41. Burger RA, Sill MW, Monk BJ, Greer BE, Sorosky JI. Phase II trial of bevacizumab in persistent or recurrent epithelial ovarian cancer or primary peritoneal cancer: a Gynecologic Oncology Group Study. *J Clin Oncol* 2007;25:5165–71.
42. Cannistra SA, Matulonis UA, Penson RT, Hambleton J, Dupont J, Mackey H, et al. Phase II study of bevacizumab in patients with platinum-resistant ovarian cancer or peritoneal serous cancer. *J Clin Oncol* 2007;25:5180–6.
43. Kumaran GC, Jayson GC, Clamp AR. Antiangiogenic drugs in ovarian cancer. *Br J Cancer* 2009;100:1–7.
44. Ledermann JA, Raja FA. Targeted trials in ovarian cancer. *Gynecol Oncol* 2010;119:151–6.
45. Chen HX, Cleck JN. Adverse effects of anticancer agents that target the VEGF pathway. *Nat Rev Clin Oncol* 2009;6:465–77.
46. Sanchez-Cespedes M, Parrella P, Esteller M, Nomoto S, Trink B, Engles JM, et al. Inactivation of LKB1/STK11 is a common event in adenocarcinomas of the lung. *Cancer Res* 2002;62:3659–62.
47. Matsumura A, Isobe T, Takano S, Kawamura H, Anno I. Non-invasive quantification of lactate by proton MR spectroscopy and its clinical applications. *Clin Neurol Neurosurg* 2005;107:379–84.

# Cancer Research

The Journal of Cancer Research (1916–1930) | The American Journal of Cancer (1931–1940)

## Glycolytic Phenotype and AMP Kinase Modify the Pathologic Response of Tumor Xenografts to VEGF Neutralization

Giorgia Nardo, Elena Favaro, Matteo Curtarello, et al.

*Cancer Res* 2011;71:4214-4225. Published OnlineFirst May 5, 2011.

<b>Updated version</b>	Access the most recent version of this article at: doi: <a href="https://doi.org/10.1158/0008-5472.CAN-11-0242">10.1158/0008-5472.CAN-11-0242</a>
<b>Supplementary Material</b>	Access the most recent supplemental material at: <a href="http://cancerres.aacrjournals.org/content/suppl/2011/05/05/0008-5472.CAN-11-0242.DC1">http://cancerres.aacrjournals.org/content/suppl/2011/05/05/0008-5472.CAN-11-0242.DC1</a>

<b>Cited articles</b>	This article cites 46 articles, 16 of which you can access for free at: <a href="http://cancerres.aacrjournals.org/content/71/12/4214.full.html#ref-list-1">http://cancerres.aacrjournals.org/content/71/12/4214.full.html#ref-list-1</a>
<b>Citing articles</b>	This article has been cited by 5 HighWire-hosted articles. Access the articles at: <a href="/content/71/12/4214.full.html#related-urls">/content/71/12/4214.full.html#related-urls</a>

<b>E-mail alerts</b>	<a href="#">Sign up to receive free email-alerts</a> related to this article or journal.
<b>Reprints and Subscriptions</b>	To order reprints of this article or to subscribe to the journal, contact the AACR Publications Department at <a href="mailto:pubs@aacr.org">pubs@aacr.org</a> .
<b>Permissions</b>	To request permission to re-use all or part of this article, contact the AACR Publications Department at <a href="mailto:permissions@aacr.org">permissions@aacr.org</a> .